J Mater Sci (2023) 58:4541–4551

Energy materials

Achieving high Li^+ diffusion in reduced graphene oxide/$NaTi_2(PO_4)_3$ heterostructures for enhanced lithium ions storage

Yaxuan He[1] and Haibo Li[1,*]

[1] Ningxia Key Laboratory of Photovoltaic Materials, School of Materials and New Energy, Ningxia University, Yinchuan 750021, People's Republic of China

Received: 31 October 2022
Accepted: 1 February 2023
Published online: 23 February 2023

© The Author(s), under exclusive licence to Springer Science+Business Media, LLC, part of Springer Nature 2023

ABSTRACT

In this work, the reduced graphene oxide/$NaTi_2(PO_4)_3$ (rGO/NTP) nanocomposite has been prepared by employing MXene as both the template and precursor for lithium ions battery with the enhanced performance. It is found that the NTP nanoparticles compact together and tightly decorate on the rGO layer. This novel structure benefits to shorten the diffusion path of Li^+ and provide high conductivity, which are proved by the density functional calculations. Further, the Li^+ diffusion coefficient of rGO/NTP is 3.68×10^{-9} $cm^2 \cdot s^{-1}$ which is much higher than that of the NTP (7.18×10^{-10} $cm^2 \cdot s^{-1}$). The results demonstrate that the rGO/NTP anode offers the high specific discharge capacity of 400.9 $mAh \cdot g^{-1}$ after 200 cycles at 0.1 $A \cdot g^{-1}$, which is nearly twice higher than that of NTP anode. Even the current density varied from 0.1 to 2 $A \cdot g^{-1}$, the specific capacity rGO/NTP anode can reach to 149.2 $mAh \cdot g^{-1}$. Further, the integrity of the lamellar structure rGO/NTP anode remained after 200 cycles, highlighting the superior stability.

Introduction

Lithium-ion batteries (LIBs) have been extensively applied in our society, such as green energy power grid systems, electronic consumer goods and electric vehicles [1–4]. It has provided the significant advantages of high energy density, prominent specific capacity and long cycle life compared with other energy storage devices [5, 6]. Owing to the low carbon emission, electric vehicles have been calling for large-scale applications, which demand greater requirements on the performance of LIBs [7, 8]. Unfortunately, the anodes of LIBs suffer from low capacity and power density, these of which are attributed to the formation of a solid electrolyte interface (SEI) layer between the electrode and electrolyte as well as the irreversible redox reaction relating to the lithiation/de-lithiation process [9–12].

Handling Editor: Mark Bissett.

Address correspondence to E-mail: lihaibo@nxu.edu.cn

https://doi.org/10.1007/s10853-023-08270-4

Up to now, despite great efforts are devoted to designing advanced anodes, such as $Li_4Ti_5O_{12}$ [13], transition metal oxides [14, 15], silicon-derivatives [16–18] and hard carbons [19, 20], it is still a challenge to develop suitable anode material with high-rate capability, long cycling life and excellent safety.

The NASICON-type $NaTi_2(PO_4)_3$ (NTP) as a typical representative of polyanionic Ti-based materials exhibits an open 3D skeleton structure, which is conducive to the construction of a convenient and fast transmission path for Li^+ diffusion [21–24]. In the structure, the TiO_6 octahedra share all of their corners with PO_4 tetrahedra, and Li^+ occupy the interstitial sites [25]. In 1988, *Delmas* performed the pioneered work to explore the possibility of Li^+ intercalation into NTP [26]. Then, *Masquelier* reported that the stable framework of $ATi_2(PO_4)_3$ (A = Li and Na) is very beneficial to intercalate/de-intercalate Li^+ reversibly upon the cycling increases [27]. However, the separation of TiO_6 octahedrons leads to poor conductivity. Thus, the cyclic stability and rate capability of pure NTP electrode are concerning. In order to face these issues, extensive works have been dedicated to develop the nano-NTP which is expected to achieve a short diffusion path for electrons. Meanwhile, compositing carbonaceous materials with NTP is also effective to enhance the electrical conductivity [28, 29]. For example, Mao et al. prepared a carbon-coated NTP microsphere, which offered an initial capacity of 105.3 $mA{\cdot}g^{-1}$ at 5 C and a low capacity loss of about 0.018% per cycle after 2000 cycles. It realized that carbon coating favors to improve the efficient transmission of electrons between the electrolyte and electrode, and meanwhile the microspheric structure reinforces the cycling stability of NTP as well [30]. Among carbonaceous materials, the reduced graphene oxide (rGO) is envisioned to be the ideal conductive substrate [31]. Most significantly, the coupling of rGO can prevent the agglomeration of active materials during the cycling.

In this work, the 2D layered $Ti_3C_2T_x$ (T mainly represents F, OH, O functional group) was employed as Ti source and substrate to in situ prepare the NTP nanoparticles. Then, the reduced graphene oxide (rGO) was utilized to couple with NTP. The morphology, structure, density functional calculation, electrochemical behavior and Li^+ transport characteristics of rGO/NTP and NTP are comparatively explored. The findings pointed out that the synergistic effect of rGO and NTP has manifested the significant superiority to enhance the rate capability and cyclic ability.

Experimental section

Synthesis of rGO/NTP

Firstly, 1 g LiF powder was added to 20 mL HCl solution whose concentration is 9 $mol{\cdot}L^{-1}$ and then stirred for 15 min. Afterward, 1 g Ti_3AlC_2 powder was poured into the above solution and stirred at 40 °C for 96 h using magnetic heating agitator to remove the Al layer. Subsequently, the resultant solution was washed and centrifuged with deionized water (DI) until the pH value exceeded 6. Then, 20 mL DI was added to the precipitate, accompanied by performing the ultrasonication for 2 h and centrifuging at 3500 r/min under room temperature for 1 h. Finally, the few layered $T_3C_2F_x$ were obtained by freeze-drying the supernatant. Secondly, 429.36 mg $NH_4H_2(PO_4)_3$ and 66.25 mg Na_2CO_3 were dissolved in 10 mL DI to obtain solution A. Then, 0.1 g $Ti_3C_2T_x$ was added into 20 mL DI to obtain solution B. solution A was slowly dropped into solution B for 2 h, accompanied by stirring. After that, the mixture was stirred vigorously in a water bath at 70 °C until the gel was formed. Then, it was freeze-dried. The resultant product was annealed at 350 °C for 2 h and then performed the second annealing at 700 °C for 6 h to obtain NTP. Successfully, the NTP and rGO were mixed with ultrasound at a mass ratio of 1:1 and then freeze-dried, and followed by heating at 280 °C for 3 h under Ar atmosphere to obtain the rGO/NTP.

Materials characterization

The scanning electron microscopy (SEM; Hitachi SU5000, Japan) and high-resolution transmission electron microscopy (HRTEM; FEI Talos200s, USA) were employed to observe the morphologies and microstructures of samples. Regarding the phase identification, the X-ray diffraction (XRD; Smart Lab, Japan) was utilized (2θ = 5°–80°). X-ray source is *K* alpha 1 ray using Cu target, where the power of *K* alpha 1 is 2 KW. The Raman spectrum was characterized by the Raman Spectrometer (USA DXR). Moreover, the laser wavelength is 532 nm and the irradiation length is 60–9000 cm^{-1}. The Fourier

transform infrared spectrometer (FTIR; spectrum Two03040404, USA) was performed with KBr pellets. The Brunauer–Emmett–Teller (BET) and Barrett–Joyner–Halenda (BJH) methods was adopted to determine the SSA and pore size distributions using a surface area analyzer (JW-BK200C, China). X-ray photoelectron spectroscopy (XPS, Thermo ESCALAB 250Xi) was carried out to investigate the surface chemical structure composition.

Electrochemical measurements

The electrochemical behavior of the samples was analyzed by fabricating the lithium half cells made in the Ar-filled glove box. Essentially, the 80% NTP/rGO, 10% conductive carbon black and 10% polyvinylidene difluoride (PVDF) were completely mixed by adding few drops of N-methyl pyrrolidone (NMP) solution. Then, the resultant slurry was uniformly pasted on the copper current collectors. Afterwards, the residual NMP within the as-prepared electrode was removed by heating at 80 °C for 12 h. The 1 M $LiPF_6$ dissolved in the mixture of ethylene carbonate, diethyl carbonate and ethyl methyl carbonate (1:1:1 wt%) was employed as the electrolyte. In terms of the electrochemical measurement, the constant current charge–discharge profiles of the LIBs cells were obtained on a battery measurement system (CT2001A, LANHE, China). Further, the electrochemical impedance spectrum (EIS) and cyclic voltammetry (CV) curves were performed by an electrochemical workstation (PARSTAT 3000A-DX, Princeton Applied Research, USA).

Theoretical calculations

The Vienna Ab Initio Package (VASP) was employed to achieve the density functional theory (DFT) calculation. It is based on the generalized gradient approximation (GGA) using the Perdew, Burke and Enzerhof (PBE) formulation [32–34]. Further, the Brillouin zone was set with a Monkhorst–Pack $2 \times 2 \times 1$ k-point grid and integrated by using Gaussian method with a smearing width of 0.05 eV. The convergence criteria for energy and force were separately defined as 10^{-5} eV and 0.05 eV/Å, assuring that the electronic energy was considered self-consistent as well as a convergent geometry optimization. The projected augmented wave (PAW) potentials were applied to describe the ionic cores and took valence electrons into account using a plane wave basis set with a kinetic energy cutoff of 450 eV [35, 36]. Partial occupancies of the Kohn–Sham orbitals were allowed using the Gaussian smearing method and a width of 0.05 eV. The dispersion interactions were described by using Grimme's DFT-D3 methodology [37].

Results and discussion

Figure 1 depicts the schematical synthesis process of rGO/NTP. The precursor is obtained by adding an appropriate amount of $NH_4H_2(PO_4)_3$ and Na_2CO_3 to $Ti_3C_2T_x$ solution and followed by withstanding freeze-drying. Then, it was sintered in a muffle furnace to achieve the NTP. In this process, the $NH_4H_2(PO_4)_3$ was decomposed to NH_3 and H_3PO_4 at 300 °C. Then, H_3PO_4 reacted with $Ti_3C_2T_x$ and Na_2CO_3 to form NTP as the temperature goes up. All related reactions are given as below:

$$NH_4H_2PO_4 \rightarrow NH_3 + H_3PO_4 \quad (1)$$

$$H_3PO_4 + Na_2CO_3 + Ti^{3+} \rightarrow NaTi_2(PO_4)_3 + CO_2 + H_2O \quad (2)$$

Finally, the NTP and GO were coupled by ultrasonic mixing. Enabling the reduction, the GO/NTP was sent into the tube furnace to reduce at 280 °C to get rGO/NTP. It is expected that the rGO favors to promote the electron transition and Li^+ diffusion, resulting in high specific capacity and prominent rate capability.

Figure 2a shows the SEM image of $Ti_3C_2T_x$ which displays the typical layered structure. Figure 2b exhibits the SEM image of NTP. The NTP nanoparticles aggregated together to form the layered framework. Most importantly, the layered NTP structure can effectively shorten the migration path of Li^+. Meanwhile, the inherent stress released from the NTP during the charge–discharge can be alleviated along with the widthwise direction. When coupling with the rGO, the rGO uniformly covers the NTP, as shown in Fig. 2c. Such structure favors to enhance the conductivity of the whole electrode as well as promotes the electron transfer during the charge–discharge process. Figure 2d and e shows the TEM and HRTEM image of rGO/NTP, respectively. It again confirms that the NTP nanoparticles are tightly attaching on the rGO layer. Further, the lattice

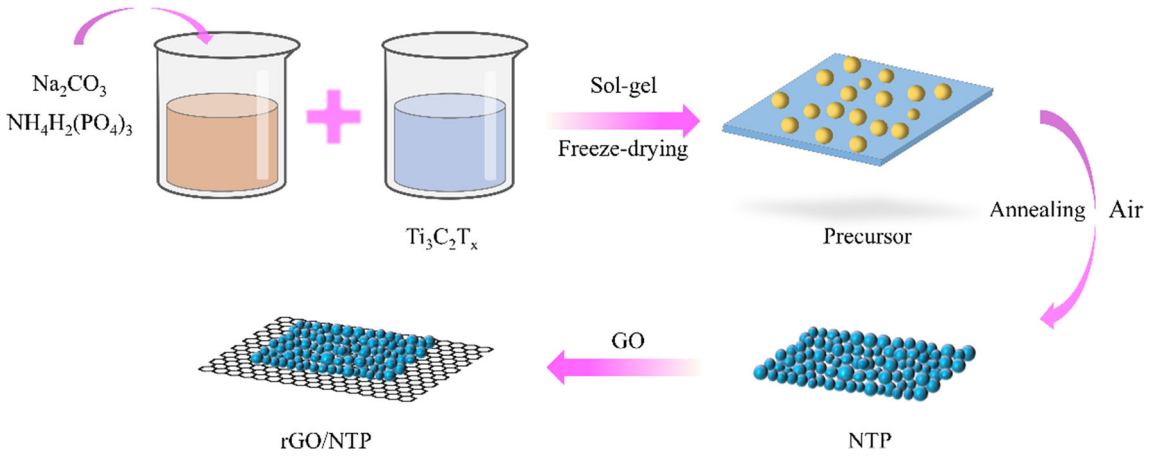

Figure 1 Schematic illustration of the synthetic process for rGO/NTP.

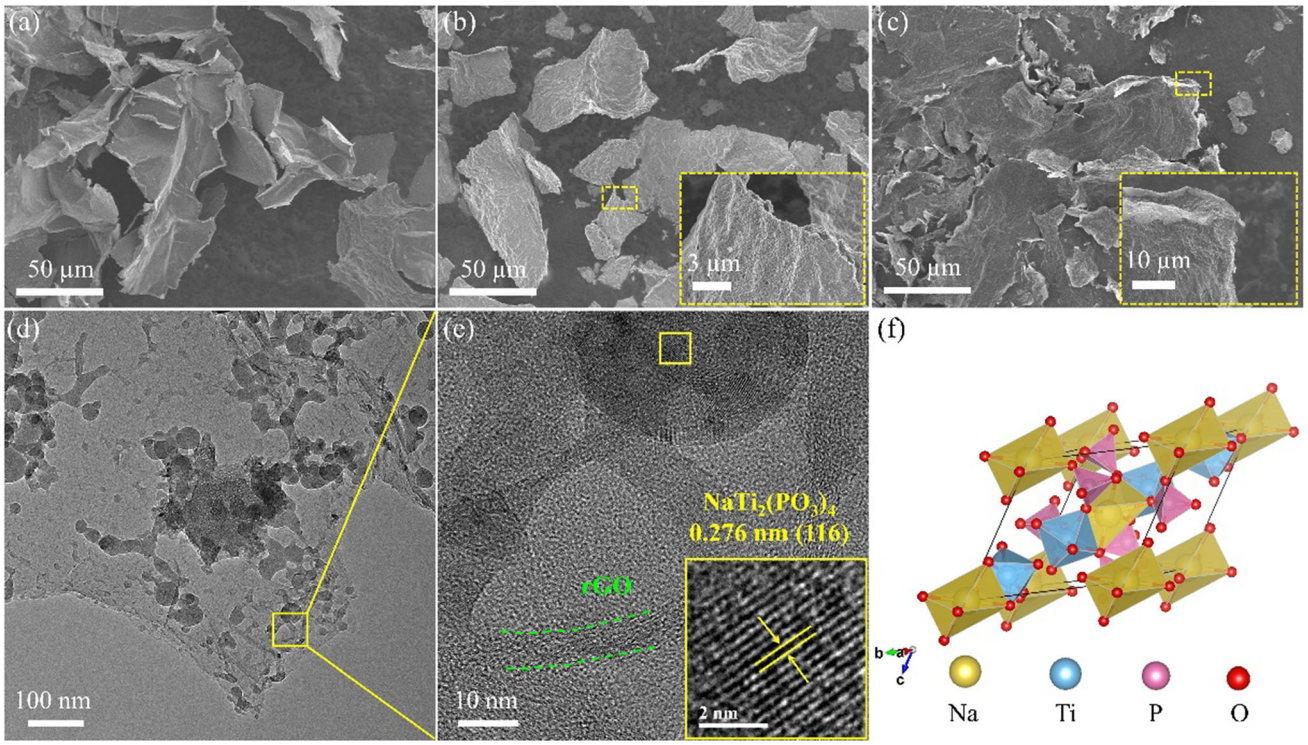

Figure 2 SEM images of **a** $Ti_3C_2T_x$, **b** NTP and **c** rGO/NTP, **d** TEM and **e** HRTEM image of rGO/NTP, **f** the crystal structure of NTP.

spacing equals to 0.276 nm can be captured which belongs to the (116) diffraction plane of NTP. In the meanwhile, the lattice fringe corresponding to rGO is examined as well. Figure 2f draws the crystal structure of NTP. It obviously demonstrated that NTP is constituted by connecting TiO_6 octahedron and PO_4 tetrahedron [38, 39]. Such an open 3D structure is very conducive to the transmission of Li^+.

The XRD patterns of $Ti_3C_2T_x$, NTP and rGO/NTP are shown in Fig. 3a. Essentially, the characteristic diffraction peaks of $Ti_3C_2T_x$ match with the reported data very well. Further, the XRD patterns of the NTP and rGO/NTP can be precisely indexed by the standard card (PDF#84-2009). Significantly, the high intensity of the diffraction peak indicates the good crystallinity. The main diffraction peaks are found at 14.4°, 20.2°, 20.9°, 24.2°, 25.3°, 29.3° and 32.4° corresponding to the (012), (104), (110), (113), (202), (024) and (116) planes of NTP. After coupling with rGO, the characteristic diffraction peaks of NTP do not

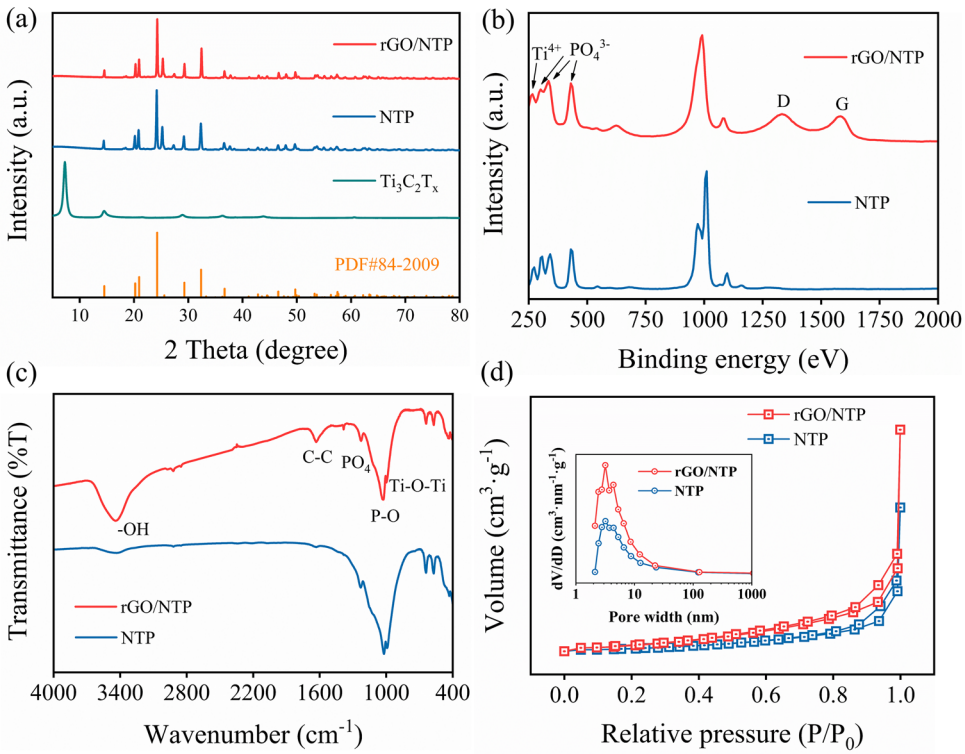

Figure 3 **a** XRD patterns, **b** Raman spectra, **c** FTIR spectra, **d** nitrogen adsorption/desorption isotherms and pore size distribution of rGO/NTP and NTP.

obviously change. Unfortunately, no obvious diffraction peaks relating to carbon are observed, which is presumably ascribed to the low mass loading of rGO or its low crystallinity. Figure 3b exhibits the Raman spectra of rGO/NTP and NTP. From the figure, three typical peaks of NTP appeared at 972, 1010 and 1098 cm^{-1}. The peak at 273 cm^{-1} is related to the translational vibration of Ti^{4+}, while peaks at 307, 341 and 436 cm^{-1} are associating with the PO_4^{3-} [40]. In comparison to NTP, the full width at half maximum of the representative peak at 1010 eV has not changed anymore by coupling NTP with rGO, suggesting the high crystalline phase of NTP. In rGO/NTP, strong *D* and *G* peak which represents the disordered carbon and *sp*2 hybrid carbon at 1332 and 1583 cm^{-1} are observed. Further, the I_D over I_G is 1.07, suggesting the high degree of defects due to the coupling. To study the chemical interaction between NTP and rGO, the as-prepared samples were tested by FTIR. Figure 3c shows the FTIR spectra of rGO/NTP and NTP. The absorption peaks at 997 and 641 cm^{-1} are attributed to Ti–O–Ti bond of TiO_6 octahedron, while peaks at 432, 572 and 1029 cm^{-1} correspond to P–O bond of PO_4 tetrahedron. Moreover, the absorption peak at 1227 cm^{-1} is ascribed to the tensile vibration of PO_4 [41]. In the FTIR spectrum of rGO/NTP, the absorption peak at 1631 cm^{-1} in relation to C–C bond is found, which proves the presence of rGO. Figure 3d and the inset show the N_2 adsorption–desorption curve and corresponding pore size distribution of rGO/NTP and NTP. Both the rGO/NTP and NTP have typical type-IV hysteresis loops, illuminating the existence of mesopores. The SSA of rGO/NTP and NTP are 13.95 and 6.54 $m^2 \cdot g^{-1}$, respectively, featuring the coupling of rGO benefits to promote the SSA, which is conducive to enlarging the contact area between the electrode and the electrolyte. Besides, the pore sizes of rGO/NTP and NTP are mainly distributed at 3.19 and 3.202 nm.

Figure 4a shows the survey XPS spectrum of rGO/NTP, NTP and $Ti_3C_2T_x$. The signals of P 2*p*, C1*s*, Ti 2*p*, O 1*s*, and Na 1*s* could be clearly detected from the XPS spectrum of NTP and rGO/NTP. Remarkably, the intensity of C 1*s* peak of rGO/NTP is significantly higher than that of NTP and $Ti_3C_2T_x$ due to the presence of rGO. In Fig. 4b of the C 1*s* spectrum, the C–C/C=C peak at 284.5 eV is relatively higher than that of NTP. Meanwhile, the peaks at 285.1, 286 and 288.7 eV are corresponding to the C–O, C=O and O–C=O, respectively. Figure 4c shows the high-resolution spectrum of O 1*s*. Three peaks at 533.6, 532.4 and 531.4 eV are captured, which correspond to C–O bond, P–OH and Ti–O–P, respectively [25]. As can be

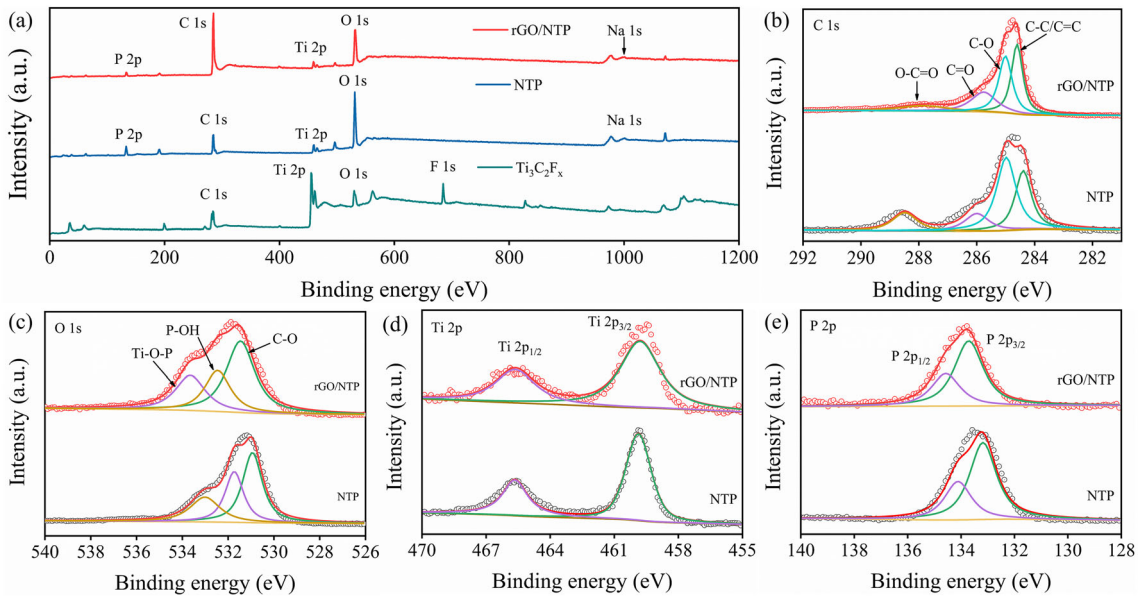

Figure 4 The **a** full XPS spectrum of rGO/NTP, NTP and $Ti_3C_2T_x$, **b** C 1*s*, **c** O 1*s*, **d** Ti 2*p* and **d** P 2*p* spectrum of rGO/NTP and NTP.

seen from Fig. 4d, the Ti 2*p* characteristic peaks in both spectrums are quite similar. Basically, Ti $2p_{3/2}$ and Ti $2p_{1/2}$ orbits locate at 459.8 eV and 465.6 eV, respectively, highlighting the Ti^{4+} [42–45]. It is observed that the binding energy of rGO/NTP shows a negative shift of 0.4 eV by compared with that of NTP, realizing the presence of chemical interaction between the rGO and NTP. In Fig. 4e, the XPS spectrum of P 2*p* can be well convolved two peaks at 134.5 and 133.7 eV, which associated with the P $2p_{1/2}$ and P $2p_{3/2}$, respectively.

Figure 5a–c shows the NTP/NTP gap structure, NTP/NTP binding structure and rGO/NTP/NTP binding structure, respectively. Correspondingly, Fig. 5d–f illuminates the charge density difference of the adsorption models. The regions in blue and yellow represent the accumulation and depletion regions of electrons, respectively. Obviously, in the NTP/NTP gap structure, there is barely accumulation of electrons. In contrast, a net excess of charges occurs in the intermediate area between NTP and NTP in Fig. 5e, which improve that the tightly connected NTP nanoparticles facilitate the diffusion of Li^+. When the surface is coupled with rGO, the accumulation of electrons is mainly distributing near to rGO, electrons prefer to transfer from the NTP surface to rGO. Figure 5g–i shows the TDOS and PDOS results of the three structures. Apparently, after coupling with rGO, the number of electrons near Fermi levels increases, which is beneficial to enhance the electronic conductivity.

Figure 6a presents the CV curve of the rGO/NTP electrode at 0.1 $mV{\cdot}s^{-1}$ from 0 to 3 V during the first four cycles. Obviously, two pairs redox peaks at 2.6/2.4 V and 0.81/0.57 V emerge which correspond to the interconversion between Ti^{4+} and Ti^{3+} and the further interconversion between Ti^{3+} and Ti^{2+}. It is noting that the interconversion of Ti^{3+} and Ti^{2+} can only be carried out in the low voltage range, and the reason for the stability of this process is that the NTP is NASICON-type structure. Figure 6b displays the cyclic performance of rGO/NTP, the high specific discharge capacity after 200 cycles is obtained as 400.9 $mAh{\cdot}g^{-1}$ at 0.1 $A{\cdot}g^{-1}$. Besides, the initial coulombic efficiency (ICE) of rGO/NTP is 51.1%. Figure 6c shows the rate capability of rGO/NTP and NTP at different current densities. From the figure, the specific discharge capacities of rGO/NTP are 408.1, 302.6, 252.9, 197.3, 149.2 and 96.8 $mAh{\cdot}g^{-1}$ at 0.1, 0.3, 0.5, 1.0, 2.0 and 5.0 $A{\cdot}g^{-1}$, respectively. When the current density recovered to 0.1 $A{\cdot}g^{-1}$, the specific discharge capacity recovered to 359.3 $mAh{\cdot}g^{-1}$. As a comparison, the specific capacities of NTP were 291.8, 210.2, 169.5, 124, 87.9, 53.5 and 238.8 $mAh{\cdot}g^{-1}$ at 0.1, 0.3, 0.5, 1, 2 and 5 $A{\cdot}g^{-1}$, respectively. In order to better study the Li^+ storage characteristics of rGO/NTP and NTP, the EIS was tested. As shown in Fig. 6d, the semicircular diameter of rGO/NTP is significantly smaller than that of NTP, indicating the

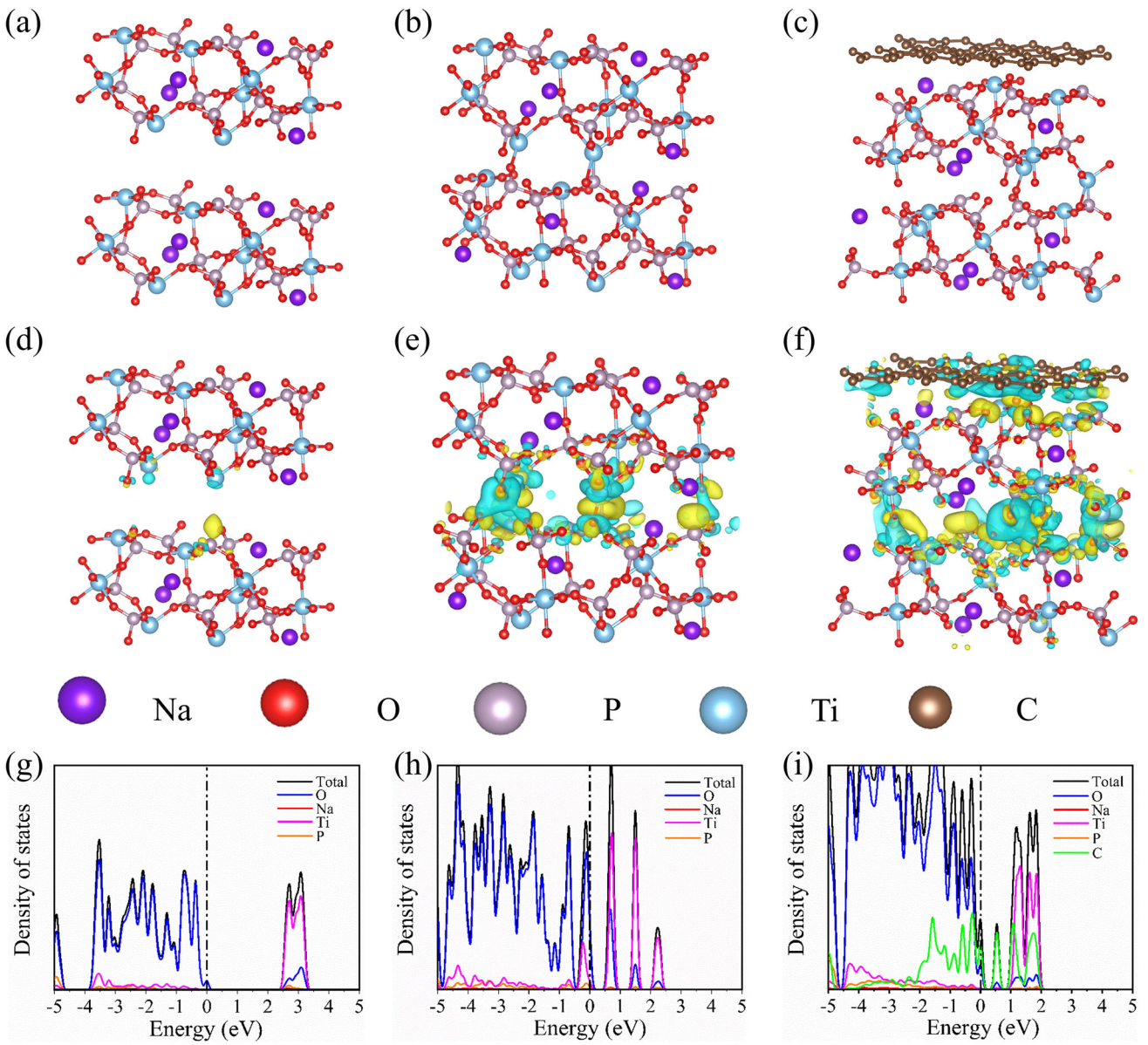

Figure 5 **a–c** the NTP/NTP gap structure, NTP/NTP binding structure, and NTP/NTP binding structure coupling with rGO, **d–f** charge density difference of the as-given adsorption models, **g–i** total and projected densities of states.

smaller charge transfer resistance. After simulation, the resistance of rGO/NTP is 156.2 Ω which is much smaller than that of NTP (443.4 Ω). In Fig. 6e, the galvanostatic intermittent titration technique (GITT) was tested by employing rGO/NTP and NTP electrodes at 0.1 $A{\cdot}g^{-1}$. The Li^+ diffusion coefficient (D_{Li+}) obtained from GITT was calculated according to the following Eq. (3) [46]:

$$D_{Li^+} = \frac{4}{\pi\tau}\left(\frac{m_B V_M}{M_B S}\right)^2 \left(\frac{\Delta E_s}{\Delta E_t}\right)^2 \quad (3)$$

where τ is the discharge/charge time, M_B and m_B are the molecular weight and the mass of active material, respectively. V_M and S represent molar volume and effective area, ΔE_s is the voltage change caused by a single pulse, ΔE_t is the total transient voltage variation during a galvanostatic charge/discharge (GCD) process. From Fig. 6f, the D_{Li+} of rGO/NTP and NTP are about 3.68×10^{-9} $cm^2{\cdot}s^{-1}$ and

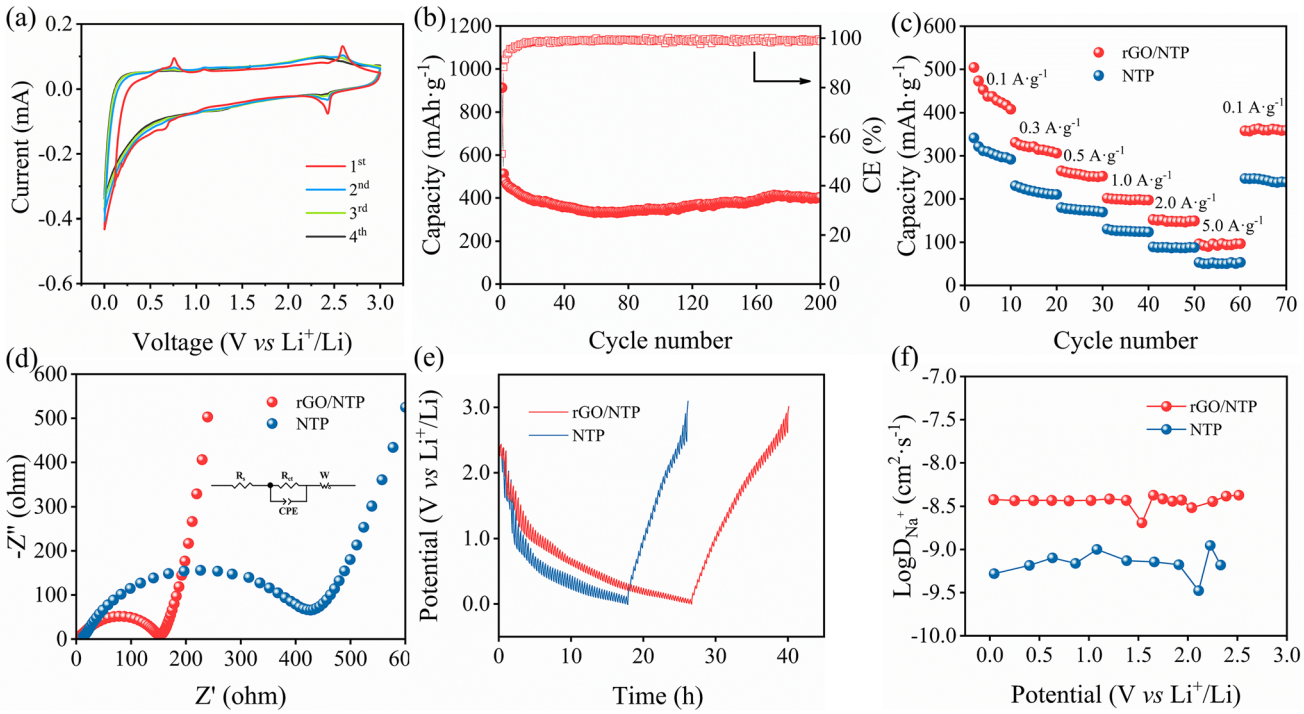

Figure 6 **a** The CV curves of rGO/NTP. The **b** cyclic performance, **c** rate capability, **d** EIS spectra, **e** GITT curves and **f** the diffusion coefficient of Li^+ during the discharge process of rGO/NTP and NTP.

7.18×10^{-10} $cm^2 \cdot s^{-1}$, respectively. The result is consistent with EIS, confirming that rGO effectively facilitates Li^+ transport kinetics of electrode material.

The morphology and structure evolution of the rGO/NTP electrode before/after the cycling were obtained to explore the Li^+ storage behavior. Figure 7a and b exhibits the cross-sectional SEM images of rGO/NTP electrode before and after 200 cycles at 0.1 $A \cdot g^{-1}$, respectively. It can be observed that the raw rGO/NTP electrode has obviously lamellar structure. After cycling, although the stacking phenomenon of electrode material occurred, it remains the integrity of the lamellar structure which promises the stable cyclic performance of the electrode. In Fig. 7c, the raw NTP electrode also has lamellar structure before cycling. However, after 200 times charge–discharge cycles, the NTP electrode has obvious agglomeration and pulverization, from Fig. 7d. This verifies the structural stability of rGO/NTP. Figure 7e and f are the TEM image and HRTEM image of rGO/NTP anode performed after 200 cycles, the 0.36 nm lattice spacing diffraction fringe was obtained, corresponding to the (113) diffraction plane of NTP. Thus, the structure stability of rGO/NTP in cycling is further verified. Beyond that, the XRD patterns of rGO/NTP after 200 cycles display two diffraction peaks at 25.2° and 33.3°, which is relating to the (113) and (116) planes of NTP, respectively.

Conclusion

In summary, the rGO/NTP nanocomposite has proposed as advanced anode for LIBs. Regarding the preparation of rGO/NTP, the MXene was employed as the template and precursor. Thus, the NTP nanoparticles tightly connected together to form the 2D lamellar structure, which effectively shorten the migration path of Li^+, resulting in enhanced capacitance at high rate. After compositing with rGO, the electronic conductivity of the rGO/NTP was significantly reinforced. When it was used as the anode for LIBs, the specific capacity reach to 400.9 $mAh \cdot g^{-1}$ after 200 cycles at 0.1 $A \cdot g^{-1}$. Even the current density increased to 2.0 $A \cdot g^{-1}$, the specific capacity still remain at 149.2 $mAh \cdot g^{-1}$. Further, it is explored that the D_{Li+} of rGO/NTP is $\sim 3.68 \times 10^{-9}$ $cm^2 \cdot s^{-1}$, whereas it is 7.18×10^{-10} $cm^2 \cdot s^{-1}$ for NTP. Remarkably, the integrity of the lamellar structure of rGO/NTP electrode is kept very well after 200 times

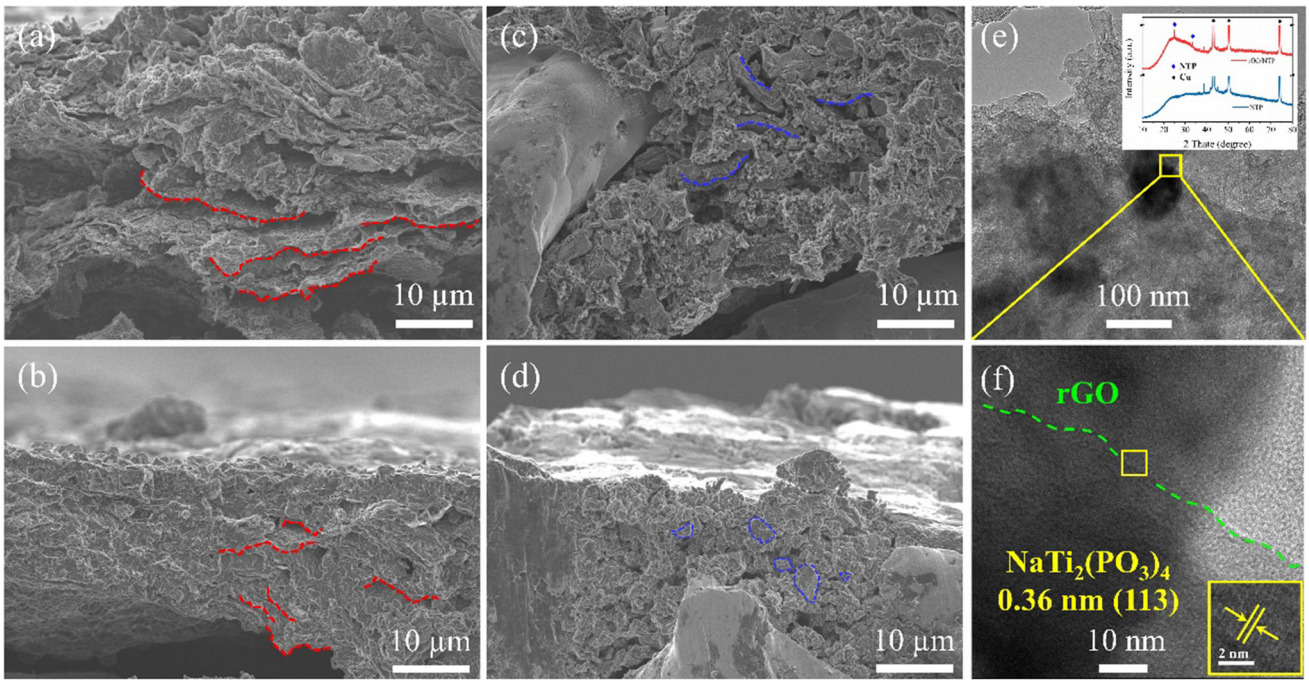

Figure 7 **a** and **b**, **c** and **d** are the cross-sectional SEM images of rGO/NTP and NTP performed before and after 200 times charge–discharge cycles, respectively. The **e** TEM image and **f** HRTEM image of rGO/NTP anode performed after 200 times charge–discharge cycles and the insert image is the corresponding XRD patterns.

charge–discharge cycles, featuring the exceptional structural stability.

Acknowledgements

This work was supported by the project of Ningxia key R&D plan (2021BEE03006).

References

[1] Deng DA (2015) Li-ion batteries: basics, progress, and challenges. Energy Sci Eng 3:385–418

[2] Meng J, Guo H, Niu C, Zhao Y, Xu L, Li Q, Mai L (2017) Advances in structure and property optimizations of battery electrode materials. Joule 1:522–547

[3] Choi JW, Aurbach D (2016) Promise and reality of post-lithium-ion batteries with high energy densities. Nat Rev Mater 1:16013–16016

[4] Liu JY, Zheng QY, Goodman MD (2016) Graphene sandwiched mesostructured Li-ion battery electrodes. Adv Mater 28:7696–7702

[5] Reddy MV, Subba RG, Chowdari B (2013) Metal oxides and oxysalts as anode materials for Li ion batteries. Chem Rev 113:5364–5457

[6] Goodenough JB, Kim Y (2015) Challenges for rechargeable Li batteries. Chem Mater 22:587–603

[7] He YX, Li HB (2022) Templated synthesis of 2D TiO_2 nanoflakes for durable lithium ion batteries. New J Chem 46:16260–16264

[8] Yi TF, Mei J, Peng PP, Luo SH (2019) Facile synthesis of polypyrrole-modified $Li_5Cr_7Ti_6O_{25}$ with improved rate performance as negative electrode material for Li-ion batteries. Comp Part B 167:566–572

[9] Dash R, Pannala S (2016) Theoretical limits of energy density in silicon-carbon composite anode based lithium ion batteries. Sci Rep 6:27449–7

[10] Zheng JX, Lu J, Amine K, Pan F (2017) Depolarization effect to enhance the performance of lithium ions batteries. Nano Energy 33:497–507

[11] Yang JH, Sagar RR, Anwar T, Li XC, Qian Z, Liang TX (2022) Graphene foam as a stable anode material in lithium-ion batteries. Int J Energy Res 46:5226–5234

[12] Qi X, Chen X, Peng SK, Wang JX, Yan SJ (2019) Research progress on two-dimensional nanomaterials MXenes and their application for lithium-ion batteries. J Mater Eng 47:10–20

[13] Zhu WJ, Yang H, Zhang WK, Huang H, Tao XY, Xia Y, Gan YP, Guo XZ (2015) Synthesis and electrochemical

performance of $Li_4Ti_5O_{12}/TiO_2$/C nanocrystallines for high-rate lithium ion batteries. RSC Adv 5:74774–74782

[14] Xiong H, Slater MD, Balasubramanian M, Johnson CS (2011) Amorphous TiO_2 nanotube anode for rechargeable sodium ion batteries. J Phys Chem Lett 2:2560–2565

[15] Senguttuvan P, Rousse G, Seznec V (2011) $Na_2Ti_3O_7$: lowest voltage ever reported oxide insertion electrode for sodium ion batteries. ChemInform 4:24109–24111

[16] Kim SH, Baek WJ, Heo S, Yun DJ, Han SS, Jung H (2018) Nanoscale electrical degradation of silicon-carbon composite anode materials for lithium-ion batteries. ACS Appl Mater Interfaces 10:24549–24553

[17] Liu CY, Zhao N, Xu K, Li YD, Mwizerwa JP, Shen J, Chen ZW (2022) High-performance $LiFePO_4$ and SiO@C/-graphite interdigitated full lithium-ion battery fabricated via low temperature direct write 3D printing. Mater Today Energy 29:101098–10

[18] Liu DQ, Liu ZJ, Li XW, Xie WH, Wang Q, Liu QM, Fu YJ, He DY (2017) Group IVA element (Si, Ge, Sn)-based alloying/dealloying anodes as negative electrodes for full-cell lithium-ion batteries. Small 13:1702000–27

[19] Zuo JL, Guo Y (2020) Formation of hard carbon derived from sulfonated pitch as advanced electrodes for lithium-ion batteries. Int J Electrochem Sci 15:3196–3203

[20] Yu HC, Dong XL, Pang Y, Wang YG, Xia YG (2017) High power lithium-ion battery based on spinel cathode and hard carbon anode. Electrochim Acta 228:251–258

[21] Liang LW, Sun X, Wu C, Hou LR, Sun JF, Zhang XG, Yuan CZ (2018) NASICON-type surface functional modification in core-shell $LiNi_{0.5}Mn_{0.3}Co_{0.2}O_2$@$NaTi_2(PO_4)_3$ cathode enhances its high-voltage cycling stability and rate capacity towards Li-ion batteries. ACS Appl Mater Interfaces 10:5498–5510

[22] Zheng W, Wu M, Yang C (2020) Carbon nanotube linked $NaTi_2(PO_4)_3$/C composite with three-dimensional conductive network as superior electrode for sodium ion battery. Ionics 26:2883–2890

[23] Xu L, Xu GB, Chen Z, Wei X (2018) 3D nanocomposite archiecture constructed by reduced graphene oxide, thermally-treated protein and mesoporous $NaTi_2(PO_4)_3$ nanocrystals as free-standing electrodes for advanced sodium ion battery. J Mater Sci Mater Electron 29:1–10

[24] Jiang Z, Zhu J, Li YH, He ZX, Meng W, Jiang YQ, Dai L, Wang L (2018) Effect of Sn doping on the electrochemical performance of $NaTi_2(PO_4)_3$/C composite. Ceram Int 44:15646–15652

[25] Roh HK, Kim HK, Kim HS, Kim DH, Chung KY, Roh KC (2016) In situ synthesis of chemically bonded $NaTi_2(PO_4)_3$/rGO 2D nanocomposite for high-rate sodium-ion batteries. Nano Res 9:1844–1855

[26] Delmas C, Nadiri A, Soubeyroux JL (1988) The nasicon-type titanium phosphates $LiTi_2(PO_4)_3$, $NaTi_2(PO_4)_3$ as electrode materials. Solid State Ionics 28:419–423

[27] Patoux S, Masquelier C (2002) Lithium insertion into titanium phosphates, silicates, and sulfates. Chem Mater 14:5057–5068

[28] Chen M, Zhou QN, Iqbal A, Nazakat A, Yan CY, Tian H, Li WQ, Zhang YC, Dong BX, Zai JT, Qian XF (2020) Self-supported $NaTi_2(PO_4)_3$ nanorod arrays: balancing Na^+ and electron kinetics via optimized carbon coating for high-power sodium-ion capacitor. ACS Appl Mater Interfaces 12:50388–50396

[29] Tang YK, Liu L, Zhang Y, Xie J, Gao Y, Zeng XY, Zhang Y (2020) Construction of the $NaTi_2(PO_4)_3$/C electrode with a one-dimensional porous hybrid structure as an advanced anode for sodium-ion batteries. Dalton Trans 49:4680–4684

[30] Mao WT, Zhang SJ, Cao FP, Pan JL, Ding YM, Ma C, Li ML, Hou ZG, Bao KY, Qian YT (2020) Synthesis of $NaTi_2(PO_4)_3$@C microspheres by an in situ process and their electrochemical properties. J Alloys Compd 842:155300–155309

[31] Guo P, Song HH, Chen XH (2009) Electrochemical performance of graphene nanosheets as anode material for lithium-ion batteries. Electrochem Commun 11:1320–1324

[32] Kresse G, Furthmüller J (1996) Efficient iterative schemes for ab initio total-energy calculations using a plane-wave basis set. Phys Rev B 54:11169–11186

[33] Perdew JP, Burke K, Ernzerhof M (1966) Generalized gradient approximation made simple. Phys Rev Lett 77:3865–3868

[34] Kresse G, Joubert D (1999) From ultrasoft pseudopotentials to the projector augmented-wave method. Phys Rev B 59:1758–1775

[35] Blöchl PE (1994) Projector augmented-wave method. Phys Rev B 50:17953–21797

[36] Grimme S, Antony J, Ehrlich S, Krieg HL (2010) A consistent and accurate ab initio parametrization of density functional dispersion correction (DFT-D) for the 94 elements H-Pu. J Chem Phys 132:154104

[37] Henkelman G, Uberuaga BP, Jonsson H (2000) A climbing image nudged elastic band method for finding saddle points and minimum energy paths. J Chem Phys 113:9901–4

[38] Liu ZX, An YF, Pang G, Dong SY, Xu CG, Mi CH, Zhang XG (2018) TiN modified $NaTi_2(PO_4)_3$ as an anode material for aqueous sodium ion batteries. Chem Eng J 353:814–823

[39] Chukova O, Nedilko S, Boiko R, Nagornyi P (2007) Spectroscopic investigation of sodium titanium orthophospates wide band red luminescence. Laser Opt 6610:159–166

[40] Burba CM, Frech R (2006) Vibrational spectroscopic study of lithium intercalation into $LiTi_2(PO_4)_3$. Solid State Ionics 177:1489–1494

[41] Li M, Liu L, Wang PQ, Li JY, Leng QY, Cao GZ (2017) Highly reversible sodium-ion storage in $NaTi_2(PO_4)_3$/C composite nanofibers. Electrochim Acta 252:523–531

[42] Roh HK, Kim HK, Roh KC, Kim KB (2014) $LiTi_2(PO_4)_3$/reduced graphene oxide nanocomposite with enhanced electrochemical performance for lithium-ion batteries. RSC Adv 4:31672–31677

[43] Ren W, Ai Z, Jia F, Zhang L, Fan X, Zou Z (2007) Low temperature preparation and visible light photocatalytic activity of mesoporous carbon-doped crystalline TiO_2. Appl Catal B 69:138–144

[44] Wu C, Kopold P, Ding YL, Aken PA, Maier J, Yu Y (2015) Synthesizing porous $NaTi_2(PO_4)_3$ nanoparticles embedded in 3D graphene networks for high-rate and long cycle-life sodium electrodes. ACS Nano 9:6610–6618

[45] Pang G, Nie P, Yuan CZ, Shen LF, Zhang XG, Li HS, Zhang CL (2014) Mesoporous $NaTi_2(PO_4)_3$/CMK-3 nanohybrid as anode for long-life Na-ion batteries. J Mater Chem A 2:20659–20666

[46] Niu YB, Xu MW, Zhang Y, Han J, Wang Y, Li CM (2016) Detailed investigation of a $NaTi_2(PO_4)_3$ anode prepared by pyro-synthesis for Na-ion batteries. RSC Adv 6:45605–45611

Publisher's Note Springer Nature remains neutral with regard to jurisdictional claims in published maps and institutional affiliations.

Springer Nature or its licensor (e.g. a society or other partner) holds exclusive rights to this article under a publishing agreement with the author(s) or other rightsholder(s); author self-archiving of the accepted manuscript version of this article is solely governed by the terms of such publishing agreement and applicable law.